JOURNAL OF THE AMERICAN CHEMICAL SOCIETY

Communication

pubs.acs.org/JACS

Direct Observation of Xe and Kr Adsorption in a Xe-Selective Microporous Metal–Organic Framework

Xianyin Chen,[†] Anna M. Plonka,[‡] Debasis Banerjee,[§] Rajamani Krishna,[∥] Herbert T. Schaef,[§] Sanjit Ghose,[⊥] Praveen K. Thallapally,*[,§] and John B. Parise*[,†,‡,⊥]

[†]Department of Chemistry, Stony Brook University, Stony Brook, New York 11794, United States

[‡]Department of Geosciences, Stony Brook University, Stony Brook, New York 11794, United States

[§]Fundamental & Computational Science Directorate, Pacific Northwest National Laboratory, Richland, Washington 99352, United States

[∥]Van't Hoff Institute for Molecular Sciences, University of Amsterdam, Science Park 904, 1098 XH Amsterdam, The Netherlands

[⊥]Photon Sciences, Brookhaven National Laboratory, Upton, New York 11973, United States

Supporting Information

ABSTRACT: The cryogenic separation of noble gases is energy-intensive and expensive, especially when low concentrations are involved. Metal–organic frameworks (MOFs) containing polarizing groups within their pore spaces are predicted to be efficient Xe/Kr solid-state adsorbents, but no experimental insights into the nature of the Xe–network interaction are available to date. Here we report a new microporous MOF (designated SBMOF-2) that is selective toward Xe over Kr under ambient conditions, with a Xe/Kr selectivity of about 10 and a Xe capacity of 27.07 wt % at 298 K. Single-crystal diffraction results show that the Xe selectivity may be attributed to the specific geometry of the pores, forming cages built with phenyl rings and enriched with polar –OH groups, both of which serve as strong adsorption sites for polarizable Xe gas. The Xe/Kr separation in SBMOF-2 was investigated with experimental and computational breakthrough methods. These experiments showed that Kr broke through the column first, followed by Xe, which confirmed that SBMOF-2 has a real practical potential for separating Xe from Kr. Calculations showed that the capacity and adsorption selectivity of SBMOF-2 are comparable to those of the best-performing unmodified MOFs such as NiMOF-74 or Co formate.

Increasing global energy demand drives the search for alternative, low-polluting sources of energy, as fossil-fuel combustion is nonsustainable from both economic and environmental perspectives. Currently, nuclear fission, with the highest energy density compared with other power sources,[1] is the leading emission-free technology for supply of base-load power. Apart from prevention of fossil-fuel-related carbon emission, it is estimated that utilization of nuclear power has prevented an average of 1.84 million air-pollution-related deaths.[2] Further development of nuclear fuel as a major energy source requires implementation of efficient and economically viable industrial-scale processes that separate and sequester highly radioactive waste during fuel rod reprocessing.[3] Reprocessing minimizes the volume of high-level radioactive waste, and among the most important steps in reprocessing is mitigation of the volume of radioactive waste. The economical separation of Xe and Kr is important in sequestering and mitigating the radioactive Kr in nuclear reprocessing technology. As radioactive ^{127}Xe has a half-life of 36.3 days, short-time storage of radioactive Kr/Xe mixtures and later separation of ^{85}Kr ($t_{1/2}$ = 10.8 years) from stable Xe would significantly reduce the volume of long-term-stored radioactive waste and provide industrially useful Xe. Efficient separation at near room temperature at very low pressure would ultimately compete with cryogenic technology currently used in nuclear reprocessing and air separation.

Xe/Kr separation using selective solid-state adsorbents is a viable alternative to cryogenic distillation, and many porous materials, including organic cages and modified zeolites such as Ag natrolite, have been extensively tested by experimental and computational methods.[4a−c] For example, Cooper and co-workers reported Xe-selective porous organic cages for which the selectivity arises from a precise size match between the rare gas and the organic cage cavity.[4a]

Metal–organic frameworks (MOFs) are a relatively new class of materials based on metal ions and organic ligands that form microporous frameworks. The variety of compositions capable of forming MOFs, along with their modification postsynthesis, facilitates the tailoring of pore geometry and chemistry for specific applications.[5] Only a handful of noble gas adsorption studies in MOFs have been presented in the literature.[6a−k] Thallapally and co-workers noted a 15% enhancement in the Xe adsorption capacity in NiMOF-74 after deposition of Ag nanoparticles.[7] They also observed a higher Xe/Kr selectivity and rationalized their results by invoking stronger interactions between polarizable Xe molecules and the well-dispersed Ag nanoparticles.

To date, only a handful of MOFs have been tested for Xe/Kr separation, and in view of the large number of suitable MOFs present in the literature, there is certainly scope for improvement through discovery of more selective materials than the

Received: March 10, 2015
Published: May 22, 2015

© 2015 American Chemical Society

DOI: 10.1021/jacs.5b02556
J. Am. Chem. Soc. 2015, 137, 7007−7010

ones studied to date.[8a−c] Because Xe/Kr separation is based on small differences in size and polarizability, it is expected that narrow pores and pores enriched with polar groups or unsaturated metal centers will increase the Xe affinity, resulting in better separation of Xe from Kr.[1,9] Despite this conclusion, there are no experimental reports on the molecular-level interactions between gas and framework, and this limits the reliability of theoretical calculations that could rapidly screen for selectivity and capacity. To better understand the optimal framework characteristics, direct study of the adsorption mechanism is essential, and experimental structural analysis provides the most detailed picture of adsorbate−adsorbent interactions.

Here we report the synthesis and Xe/Kr sorption properties of the new MOF SBMOF-2:H_2O (Stony Brook MOF-2) a robust three-dimensional (3D) porous crystalline structure containing calcium and 1,2,4,5-tetrakis(4-carboxyphenyl)-benzene. The dehydrated form, designated SBMOF-2, adsorbs Xe with a capacity of 27.07 wt % at 298 K and with a high Xe/Kr selectivity of approximately 10 at 298 K; these results are extraordinary for an unmodified MOF. We examined the Xe and Kr adsorption mechanism by interpreting the results of single-crystal X-ray diffraction (XRD) and observed significant differences for Xe versus Kr, noting differentiation between polar and nonpolar pores in SBMOF-2. Although polar pores occur in other MOFs,[9] the differentiation of sorbed gases between them, as occurs in SBMOF-2, has not been reported for MOFs.

The structure of SBMOF-2:H_2O is unusual among microporous MOFs.[10] Only half of the carboxylic groups are fully deprotonated, and the network contains half of the expected number of Ca^{2+} sites (Figure S1 in the Supporting Information). Charge balance provided by hydrogen, not heavier calcium, leads to the low density of the dehydrated material (1.192 g/cm^3), which is comparable to those of MOFs with significantly higher surface areas, such as HKUST-1 (0.879 g/cm^3) and MgMOF-74 (0.909 g/cm^3).[11] The half-deprotonated linker connects the calcium octahedra into a 3D framework with diamond-shaped channels running in the [100] direction (Figures S2 and S3). The excess of oxygen versus calcium also leads to a topology that is unusual for a MOF synthesized from s-block metals: the CaO_6 polyhedra are isolated, and no O atoms are shared between metal centers. To the best of our knowledge, SBMOF-2 is the first microporous 3D MOF network with isolated CaO_6 octahedra connected by linkers.

Thermogravimetric analysis (TGA) (Figure S4) indicated that as-synthesized SBMOF-2:H_2O contains 6.5 wt % water, which can be removed by heating to 513 K in vacuum. Single-crystal and powder XRD experiments (Figure S5 and Table S1) showed that water is disordered over sites within channels and that SBMOF-2 retains its structure after dehydration, with a small change of ∼3% in the unit cell volume. The accessible void space is 25.6% of the unit cell (212.5 Å^3 out of 831.4 Å^3, calculated with PLATON[12]). The two different types of channels, designated as type-I and type-II in Figure 1, have walls built with phenyl rings with delocalized π-electron clouds and H atoms pointing into the channel, providing potential sorption sites for gas molecules. The polar −OH groups are found exclusively in channels of type-II and serve as more polarizing parts in the network, resulting in significantly higher occupancy of the adsorbed noble gases. The void spaces of the type-I and type-II channels are 13.6% and 12% of the unit cell, respectively. Brunauer−Emmett−Teller measurements showed that SBMOF-2 has a moderate surface area of 195 m^2/g; the N_2 adsorption isotherm at 77 K is shown in Figure S6.

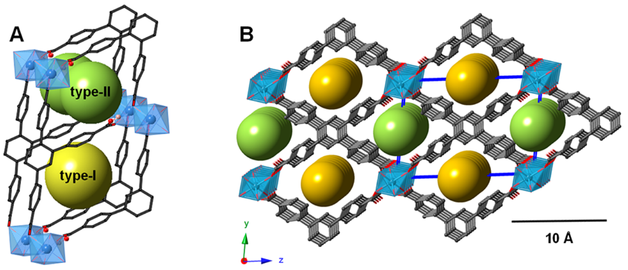

Figure 1. (A) Structure of activated SBMOF-2. The colored spheres indicate estimated channel apertures, 6.34 Å for channel type-I (yellow) and 6.66 Å for channel type-II (green). (B) Pores running along the [100] direction. Calcium octahedra are presented as blue polyhedra, oxygen atoms as red spheres, and carbon as gray wire bonds. H atoms have been omitted for clarity. The unit cell is shown in blue.

Activated SBMOF-2 maintains its topology when exposed to air for 5 days, as observed from TGA and powder XRD patterns (Figures S7 and S8). Additionally TGA measurements showed that SBMOF-2 does not saturate with water from air for 5 days.

The stability in air, small pore/channel size closer to the size of atomic xenon, and lightweight character of the SBMOF-2 suggested that it might possess good gas sorption and separation properties, and indeed, this material is remarkable at separating Xe from Kr. Adsorption/desorption isotherms of Xe and Kr on SBMOF-2 at 278, 288, and 298 K are shown in Figure 2A. Both gases display typical type-I adsorption isotherms, but the Xe uptake is more than 3 times higher: 2.83 mol/kg (27.07 wt %) versus 0.92 mol/kg (7.18 wt %) for Kr at 298 K. Although the uptake of Xe in SBMOF-2 is lower

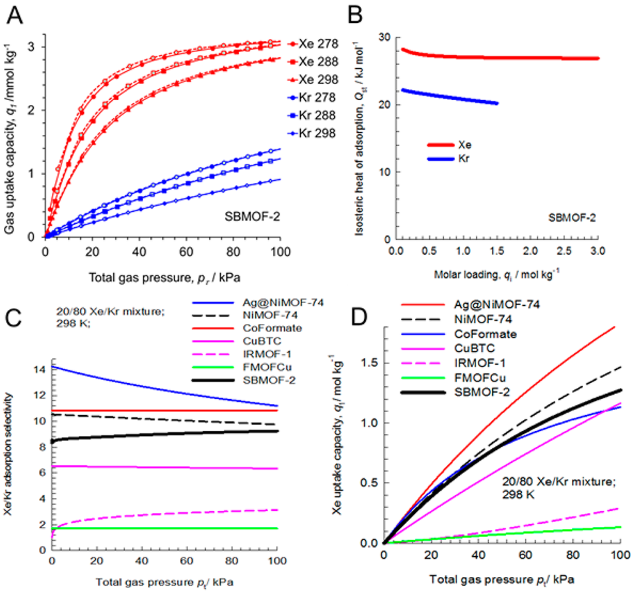

Figure 2. Kr/Xe adsorption and selectivity in SBMOF-2. (A) Single-component adsorption (solid symbols) and desorption (open symbols) isotherms of Xe (red) and Kr (blue) in SBMOF-2 collected at 278, 288, and 298 K. (B) Isosteric heats of adsorption for Xe/Kr@SBMOF-2. Calculated (C) adsorption selectivities and (D) Xe uptake capacities for 20/80 Xe/Kr mixtures in SBMOF-2 and comparison with other compounds.[1]

DOI: 10.1021/jacs.5b02556
J. Am. Chem. Soc. 2015, 137, 7007−7010

than what is observed for well-known noble gas adsorbents with open metal sites, such as NiMOF-74 and Ag@Ni-MOF74 (3.6 and 4.8 mol/kg, respectively),[6d,7] structures with open metal sites usually suffer from water sensitivity. The uptake is higher than those of Co formate (2 mol/kg) and organic cages (2.69 mol/kg), which do not have open metal sites.[4a,8b] The Xe isotherm approaches saturation at 1 bar with a gas occupancy of 1.68 molecules per unit cell at 298 K, which corresponds to a maximum of two gas molecules per unit cell, suggesting that Xe is ordered on specific sorption sites.

The isosteric heats of adsorption (Q_{st}) of the noble gases on the SBMOF-2 network were determined by analysis of the gas isotherms. Both Xe and Kr isotherm data at 278, 288, and 298 K were fitted with the dual-Langmuir−Freundlich model (Figure S9 and Table S2), and the Q_{st} values were calculated using the Clausius−Clapeyron equation. As expected, the value for Xe adsorption is higher than that for Kr (26.4 vs 21.6 kJ/mol; Figure 2B), indicating stronger binding.

Single-crystal diffraction results indicated Xe ordering with two distinct adsorption sites in channels of type-I and type-II. The absorption of 1.45 molecules per unit cell determined from diffraction agrees with the value of 1.68 molecules per unit cell determined from isotherm measurements (Figure 2A). The lower interaction potential for Kr, resulting from its smaller size and polarizabilty, explains the lower Kr occupancy (0.51 vs 0.66 from the isotherms) at 1 atm. In the structures of both SBMOF-2:Xe and SBMOF-2:Kr, the occupancy of gas atoms in channels of type-I is lower than that in channels of type-II because of the more polarizing −OH groups present in the latter.

In type-I channels, Xe is surrounded by H atoms from phenyl rings with a shortest Xe···H distance of 3.268(9) Å, while in type-II channels the shortest Xe···H and Xe···O distances are 3.646(6) and 3.567(5) Å, respectively (Figure 3). The average Xe···H distance of 3.568(8) Å in the channels of SBMOF-2:Xe is slightly shorter than the average Xe···H contact distance in the literature (3.71(4) Å),[4a] suggesting that the small pore apertures increase the energy of network−gas interactions by surrounding Xe with many H atoms in close proximity. Kr occupies two sorption sites similar to those found for SBMOF-2:Xe, with the shortest Kr···H distance of 3.342(3) Å in type-I channels and Kr···H and Kr···O distances of 3.545(3) and 3.364(4) Å, respectively, in type-II channels. The observed longer distances between H and Kr atoms in comparison with those between H and Xe atoms is consistent with the Xe selectivity in SBMOF-2 being driven by the larger size and stronger polarizability of Xe atoms compared with Kr. The observed Xe···Xe contact distance of 5.1812(3) Å is longer than in both crystalline Xe (4.3 Å) and high-pressure-induced Xe dimers.[13a−c] Similar adsorption sites were observed in a Kr-loaded structure with a Kr···Kr distance of 5.11(1) Å.

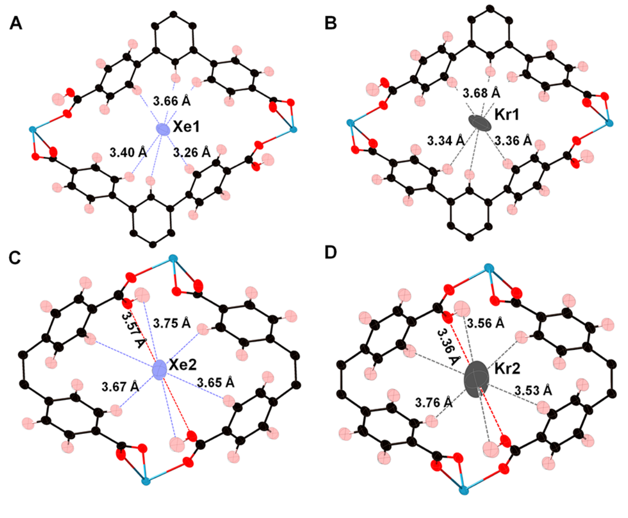

Figure 3. (A, C) Xe and (B, D) Kr sorption sites determined from single-crystal XRD experiments. The site positions of Xe and Kr in the two channels are similar, with both located at (0.5, 0, 0.5) and (0.5, 0.5, 0).

The SBMOF-2 Xe/Kr selectivity and Xe capacity for the 20/80 mixtures at 298 K were calculated with the ideal adsorbed solution theory (IAST) of Mayers and Prausnitz[14] using fitted isotherms. The results are presented in Figure 2C,D. For comparison purposes, the corresponding data for NiMOF-74, Ag@NiMOF-74, CuBTC, IRMOF-1, FMOF-Cu, and Co formate are also included. At 100 kPa, SBMOF-2 shows a Xe/Kr adsorption selectivity of about 10, comparable to the value for NiMOF-74.[6a,7]

Simulated breakthrough is commonly calculated to estimate the separation of Xe/Kr mixtures. For a 20/80 Xe/Kr feed mixture at 100 kPa and 298 K, Figure S10A shows the reduced concentrations at the outlet of a fixed bed adsorber as a function of the dimensionless time $\tau = tu/L\varepsilon$. On the basis of the outlet gas compositions, we can determine the concentration of Xe in the outlet gas as a function of τ (see Figure S10B). The corresponding data for NiMOF-74, Ag@NiMOF-74, CuBTC, IRMOF-1, FMOF-Cu, and Co formate are also included for comparison purposes. On the basis of Figure S10B, the breakthrough time for SBMOF-2 is slightly lower than those for NiMOF-74 and Ag@NiMOF-74.

To supplement the simulated breakthrough, experimental breakthrough experiments were carried out to further demonstrate the Xe/Kr separation ability for both 1/1 Kr/Xe and at low gas concentration under conditions expected for spent nuclear fuel reprocessing. A 130 mg sample of SBMOF-2 was packed in a column and activated at 513 K in flowing He overnight. After the sample was cooled to room temperature, a mixture of gases (5% Kr, 5% Xe, and 90% N_2 by volume) was introduced to the column. After injection of the gas mixture, Kr broke through the column after ~20 min, followed by Xe after ~40 min, suggesting preferable adsorption and selectivity toward Xe over Kr by SBMOF-2 (Figure 4). The adsorption

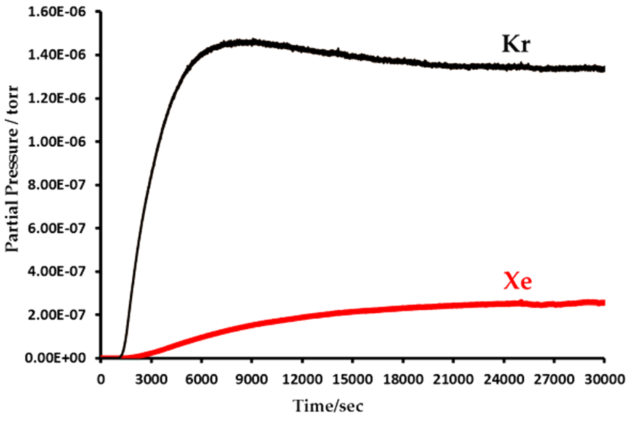

Figure 4. Breakthrough experiments showing separation of Xe and Kr at 5% Kr and 5% Xe in N_2.

capacity of Xe (0.80 mol/kg) in the column breakthrough experiments matched the Xe adsorption via the static method (0.85 mol/kg) at 0.07 bar. The experimental breakthrough measurements confirmed that the adsorption kinetics in SBMOF-2 is fast enough for separation of Xe from Kr.

In summary, the new 3D porous material SBMOF-2 has an unprecedented structure with two different hydrogen-rich channels; Xe is strongly adsorbed in pores enriched with more polarizing −OH groups. The geometry of the channels, best matched for the larger Xe atoms rather than smaller Kr, also helps explain the selectivity for Xe over Kr.

■ ASSOCIATED CONTENT

Ⓢ Supporting Information

Experimental details, simulations, and crystallographic data (CIF). The Supporting Information is available free of charge on the ACS Publications website at DOI: 10.1021/jacs.5b02556.

■ AUTHOR INFORMATION

Corresponding Authors

*john.parise@stonybrook.edu
*praveen.thallapally@pnnl.gov

Notes

The authors declare no competing financial interest.

■ ACKNOWLEDGMENTS

This work was supported by the U.S. DOE, Office of Science, Office of Basic Energy Sciences (DE-FG02-09ER46650), the DOE Office of Nuclear Energy and NSF (CHE-0840483). We acknowledge in particular J. Bresee, T. Todd (Idaho National Laboratory), and B. Jubin (Oak Ridge National Laboratory), who provided programmatic support and guidance. PNNL is a multiprogram national laboratory operated for the U.S. Department of Energy by Battelle Memorial Institute under Contract DE-AC05- 76RL01830.

■ REFERENCES

(1) Banerjee, D.; Cairns, A. J.; Liu, J.; Motkuri, R. K.; Nune, S. K.; Fernandez, C. A.; Krishna, R.; Strachan, D. M.; Thallapally, P. K. *Acc. Chem. Res.* **2015**, *48*, 211.

(2) Kharecha, P. A.; Hansen, J. E. *Environ. Sci. Technol.* **2013**, *47*, 4889.

(3) Soelberg, N. R.; Garn, T. G.; Greenhalgh, M. R.; Law, J. D.; Jubin, R.; Strachan, D. M.; Thallapally, P. K. *Sci. Technol. Nucl. Inst.* **2013**, 1.

(4) (a) Chen, L.; Reiss, P. S.; Chong, S. Y.; Holden, D.; Jelfs, K. E.; Hasell, T.; Little, M. A.; Kewley, A.; Briggs, M. E.; Stephenson, A.; Thomas, K. M.; Armstrong, J. A.; Bell, J.; Busto, J.; Noel, R.; Liu, J.; Strachan, D. M.; Thallapally, P. K.; Cooper, A. I. *Nat. Mater.* **2014**, *6*, 835. (b) Seoung, D.; Lee, Y.; Cynn, H.; Park, C.; Choi, K. Y.; Blom, D. A.; Evans, W. J.; Kao, C. C.; Vogt, T.; Lee, Y. *Nat. Chem.* **2014**, *6*, 835. (c) Bazan, R. E.; Bastos-Neto, M.; Moeller, A.; Dreisbach, F.; Staudt, R. *Adsorption* **2011**, *17*, 371.

(5) Stock, N.; Biswas, S. *Chem. Rev.* **2012**, *112*, 933.

(6) (a) Liu, J.; Thallapally, P. K.; Strachan, D. *Langmuir* **2012**, *28*, 11584. (b) Wang, H.; Yao, K.; Zhang, Z.; Jagiello, J.; Gong, Q.; Han, Y.; Li, J. *Chem. Sci.* **2014**, *5*, 620. (c) Lawler, K. V.; Hulvey, Z.; Forster, P. M. *Chem. Commun.* **2013**, *49*, 10959. (d) Thallapally, P. K.; Grate, J. W.; Motkuri, R. K. *Chem. Commun.* **2012**, *48*, 347. (e) Sikora, B. J.; Wilmer, C. E.; Greenfield, M. L.; Snurr, R. Q. *Chem. Sci.* **2012**, *3*, 2217. (f) Ueda, T.; Kurokawa, K.; Eguehit, T.; Kachi-Terajima, C.; Takamizawa, S. *J. Phys. Chem. C* **2007**, *111*, 1524. (g) Dorcheh, A. S.; Denysenko, D.; Volkmer, D.; Donner, D.; Hirscher, M. *Microporous Mesoporous Mater.* **2012**, *162*, 64. (h) Bae, Y.; Hauser, B. G.; Colón, Y. J.; Hupp, J. T.; Farha, O. K.; Snurr, R. Q. *Microporous Mesoporous Mater.* **2013**, *169*, 176. (i) Fernandez, C. A.; Liu, J.; Thallapally, P. K.; Strachan, D. M. *J. Am. Chem. Soc.* **2012**, *134*, 9046. (j) Heest, T. V.; Teich-McGoldrick, S. L.; Greathouse, J. A.; Allendorf, M. D.; Sholl, D. S. *J. Phys. Chem. C* **2012**, *116*, 13183. (k) Perry, J. J.; Teich-McGoldrick, S. L.; Meek, S. T.; Greathouse, J. A.; Haranczyk, M.; Allendorf, M. D. *J. Phys. Chem. C* **2014**, *118*, 11685.

(7) Liu, J.; Strachan, D. M.; Thallapally, P. K. *Chem. Commun.* **2014**, *50*, 466.

(8) (a) DeCoste, J. B.; Peterson, G. W. *Chem. Rev.* **2014**, *114*, 5695. (b) James, S. L. *Chem. Soc. Rev.* **2003**, *32*, 276. (c) Chae, H. K.; Siberio-Pérez, D. Y.; Kim, J. C.; Go, Y.; Eddaoudi, M.; Matzger, A. J.; O'Keeffe, M.; Yaghi, O. M. *Nature* **2004**, *427*, 522.

(9) Magdysyuk, O. V.; Adams, F.; Liermann, H. P.; Spanopoulos, I.; Trikalitis, P. N.; Hirscher, M.; Morris, R. E.; Duncan, M. J.; McCormick, L. J.; Dinnebier, R. E. *Phys. Chem. Chem. Phys.* **2014**, *16*, 23908.

(10) Zhu, Q. L.; Xu, Q. *Chem. Soc. Rev.* **2014**, *43*, 5468.

(11) He, Y.; Zhou, W.; Krishna, R.; Chen, B. *Chem. Commun.* **2012**, *48*, 11813.

(12) Spek, A. L. *Acta Crystallogr.* **2009**, *D65*, 148.

(13) (a) Somayazulu, M.; Dera, P.; Goncharov, A. F.; Gramsch, S. A.; Liermann, P.; Yang, W.; Liu, Z.; Mao, H. K.; Hemley, R. J. *Nat. Chem.* **2010**, *2*, 50. (b) Natta, G.; Nasini, A. G. *Nature* **1930**, *125*, 457. (c) Sears, D. R.; Klug, H. P. *J. Chem. Phys.* **1962**, *37*, 3002.

(14) Myers, A. L.; Prausnitz, J. M. *AIChE J.* **1965**, *11*, 121.

Supplementary Information for

Direct Observation of Xe and Kr Adsorption in a Xe-selective Microporous Metal Organic Framework

Xianyin Chen[1], Anna M. Plonka[2], Debasis Banerjee[3], Rajamani Krishna[4], Herbert T. Schaef [3], Sanjit Ghose[5], Praveen K. Thallapally[3,*] and John B. Parise[1,2,5*]

[1]Department of Chemistry, Stony Brook University, Stony Brook, NY 11794, USA
[2]Department of Geosciences, Stony Brook University, Stony Brook, NY 11794, USA
[3]Fundamental & Computational Science Directorate, Pacific Northwest National Laboratory, Richland, WA- 99352, USA
[4]Van‘t Hoff Institute for Molecular Sciences, University of Amsterdam, Science Park 904, 1098 XH Amsterdam, The Netherlands
[5]Photon Sciences, Brookhaven National Laboratory, Upton, NY 11973, USA

Correspondence to: john.parise@stonybrook.edu ; praveen.thallapally@pnnl.gov

Contents

I. Experimental Section

1. Synthesis Method

SBMOF-2:H_2O was synthesized under solvothermal conditions using Teflon-lined 23-mL Parr® stainless steel autoclaves. Starting materials include calcium chloride ($CaCl_2$, 96%, Acros-Organics), 1,2,4,5-Tetrakis(4-carboxyphenyl)benzene (TCPB) ($C_{34}H_{22}O_8$, Sigma Aldrich, 98%) and ethanol (95%, Fisher Scientific) and were used without further purification. A mixture of 0.25 mmoles of $CaCl_2$ (0.027g) and 0.05 mmoles of TCPB (0.03g) were dissolved in 12 gram of ethanol and stirred for 2 hours to achieve homogeneity. The resultant solution was heated at 373 K for 3 days. Colorless prism crystals were recovered as products and washed with ethanol. The water molecules in the structure come from the 95% ethanol solvent and adsorbed moisture in the $CaCl_2$ reactant. The yield was 50% based on the linker, 0.02g.

2. Structure of SBMOF-2:H_2O and SBMOF-2

As-synthesized SBMOF-2:H_2O crystallizes in triclinic crystal system, space group *P*-1. Calcium is coordinated to six oxygen atoms from six independent linkers, forming isolated CaO_6 octahedra, which are bridged by the carboxylic groups of the linker, resulting in a porous framework. The linker is coordinating to six calcium ions in a monodentate mode. Uncoordinated -OH groups on carboxylates in type-II channels leaves a tendency of forming hydrogen bonds along the aperture. H4 atom remains for charge balance of SBMOF-2:H_2O. (Figure S2)

Porous MOFs with calcium polyhedra have been reported as 3-D structures of edged shared polyhedra, corner shared calcium octahedral chain, edged shared tetramers, and 2-D edged shared polyhedral chain. To the best of our knowledge, SBMOF-2 is the first porous 3-D example of isolated CaO_6 octahedra connected by linkers.

3. Thermogravimetry Analysis

TGA data of SBMOF-2:H_2O and SBMOF-2 were collected using a STA 449 C Jupiter Netzsch Instrument. Powder samples were placed in alumina crucible and heated from 298 K to 1023 K with a heating rate of 10 K/min under N_2 atmosphere.

4. Xe/Kr Gas Loading and Adsorption Analysis

Fresh crystals of SBMOF-2:H_2O were activated at 513 K and hold in vacuum for 5 hours and then were placed in a three-neck flask with gas (Xe/Kr) flowing into the flask. After that, the crystals were coated with Paratone® oil, keeping gas flowing to maintain 1 atm of gas, and representative crystal was chosen for single crystal diffraction.

Xenon (Xe) and krypton (Kr) adsorption/desorption isotherms were measured using a Micromeritics ASAP 2020 volumetric adsorption analyzer. Powder samples were degassed offline at 513 K for 10 hours under dynamic vacuum (10-5 bar) before analysis, followed by degassing on the analysis port under vacuum, also at 513 K.

5. Single Crystal and Powder X-ray Crystallography

Representative crystals of fresh, activated and gases loaded samples suitable for single crystal X-ray diffraction were selected from the bulk and were mounted in Paratone® oil on CryoLoop®. Data for compounds SBMOF-2, SBMOF-2:Xe and SBMOF-2:Kr were collected with 1°ω-scans at 100 K (SBMOF-2:H_2O at room temperature) using a four-circle kappa Oxford Gemini diffractometer equipped with an Atlas detector (λ= 0.71073/1.54184Å) (Table S1). The raw intensity data were collected, integrated, and corrected for adsorption effects using CrysAlisPRO software. Data sets were corrected for absorption using a multi-scan method, and structures were solved by direct methods using SHELXS-97[1] and refined by full-matrix least squares on F^2 with SHELXL-97.[2] Atoms belonging to the framework were located first, and refined aniostropically. Hydrogen atoms were added to the structure model using geometrical constraints (HFIX command). After obtaining satisfactory model of the framework, gas atoms (Xe, Kr) were located from Fourier difference map and refined anisotropically with the occupancy refined.

Electron density maps calculated from single crystal diffraction data indicate strong ordering of Xe and Kr inside the pores (Figure S11). Furthermore, in the case of Xe we ob-served a large difference between levels of electron density in channel-II vs. channel-I (17.7 vs. 12.2 e/Å3 indicating stronger affinity of Xe for polarizing –OH groups rather than phenyl rings. Electron density maps for the Kr-adduct indicate that Kr is not as strongly differentiated between type-II and -I channels (4.0 vs. 3.3 e/Å3).

To confirm phase purity PXRD data were collected using a Rigaku Ultima-IV diffractometer Cu Kα (λ = 1.5418 Å) with a range of $5° \leq 2\theta \leq 40°$ (scanning rate: 1°/min). The powder patterns so collected were consistent with those simulated based on structure models derived from single crystal data (Figure S5). Full details of the structure determinations have been deposited with Cambridge Crystallographic Data Center under reference numbers CCDC 1039468-1039471 (specifically CCDC 1039468, SBMOF-2:H_2O; CCDC 1039469, SBMOF-2; CCDC 1039470 SBMOF-2:Xe; CCDC 1039471, SBMOF-2:Kr), and are available free of charge from CCDC.

6. Breakthrough Experiments

For the breakthrough measurements 130 mg of SBMOF-2 was packed in a 6.35 cm long and 0.5-cm diameter column. The sample was activated at 513 K under flowing helium overnight. Pressurization of the 0.25" (6.35 mm) diameter column packed with SBMOF-2 was accomplished with a syringe pump (Teledyne ISCO) directly connected to the system through a series of 0.07 mm (ID) segments of tubing (PEEK) and valves. System pressure was maintained by coordinated adjustments to the syringe pump flow rate and the needle metering valve (Tescom). An inline pressure transducer was used to verify column pressure. The column was cooled to room temperature and a mixture of 5% Kr and 5% Xe and 90% N_2 was introduced with a flow rate of 1 ml/min at a total pressure of 20 psi (1.36 atm). Effluent gas chemistry was tracked with a Stanford Research residual gas analyzer (RGA). Masses (a.m.u.) corresponding to N_2 (28), Xe

(131) and Kr (84) were monitored throughout the experiments. The flow rate (1 ml/min) through the needle metering valve created a sampling pressure of 1.0 to 3.0×10^{-4} Torr in the RGA and was maintained throughout the experiments. Indications of Xe and Kr breaking through the column were indicated by an increase in the pressure for masses 131 and 84 respectively. (See Figure S12)

II. Calculations

7. Langmuir-Freundlich Fitting of Pure Component Isotherms

The experimentally measured loadings for Xe and Kr in SBMOF-2 were measured as a function of the absolute pressure at three different temperatures 278 K, 288 K, and 298 K.

The isotherm data were fitted with the Langmuir-Freundlich model.

$$q = q_{sat} \frac{bp^{v}}{1+bp^{v}} \tag{1}$$

with T-dependent parameter b

$$b = b_0 \exp\left(\frac{E}{RT}\right) \tag{2}$$

Table S2 provides the Langmuir-Freundlich fit parameters for adsorption of Xe and Kr in SBMOF-2. Figure S9 provides a comparison of the pure component isotherm data for (a) Xe, (b) Kr in SBMOF-2 with the fitted isotherms (shown by continuous solid lines) at 278 K, 288 K, and 298 K. The fits are good for both components at all three temperatures.

8. Isosteric Heat of Adsorption

The isosteric heat of adsorption, Q_{st}, defined as:

$$Q_{st} = RT^2 \left(\frac{\partial \ln p}{\partial T}\right)_q \tag{3}$$

were determined using the pure component isotherm fits using the Clausius-Clapeyron equation. (Figure 2B)

9. IAST Calculation of Adsorption Selectivity and Uptake Capacities.

The selectivity of preferential adsorption of component 1 over component 2 in a mixture containing 1 and 2, perhaps in the presence of other components too, can be formally defined as:

$$S_{ads} = \frac{q_1/q_2}{p_1/p_2}$$

(4)

In equation (4), q_1 and q_2 are the *absolute* component loadings of the adsorbed phase in the mixture. These component loadings are also termed the uptake capacities. In all the calculations to be presented below, the calculations of q_1 and q_2 are based on the use of the Ideal Adsorbed Solution Theory (IAST) of Myers and Prausnitz.[3]

10. Transient Breakthroughs in Fixed Bed Adsorbers

The separation of Xe/Kr mixtures is commonly carried out in fixed bed adsorbers in which the separation performance is dictated by a combination of three separate factors: (a) adsorption selectivity, (b) uptake capacity, and (c) intra-crystalline diffusivities of guest molecules within the pores. Transient breakthrough simulations are required for a proper evaluation of MOFs; the simulation methodology used in our work is described in earlier publications.[4,5]

The breakthrough characteristics for any component is essentially dictated by two sets of parameters: (a) The characteristic contact time $\frac{L}{v} = \frac{L\varepsilon}{u}$ between the crystallites and the surrounding fluid phase, and (b) $\frac{Đ_i}{{r_c}^2}$, that reflect the importance of intra-crystalline diffusion limitations. It is common to use the dimensionless time, $= \frac{tu}{L\epsilon}$, obtained by dividing the actual time, t, by the characteristic time, $\frac{L\varepsilon}{u}$ when plotting simulated breakthrough curves.[4]

If the value of $\frac{Đ_i}{r_c^{2}}$ is large enough to ensure that intra-crystalline gradients are absent and the entire crystallite particle can be considered to be in thermodynamic equilibrium with the surrounding bulk gas phase at that time t, and position z of the adsorber. The assumption of thermodynamic equilibrium generally results in sharp breakthroughs for each component; sharp breakthroughs are desirable in practice because this would result in high productivity of pure products. When intra-crystalline diffusion effects are significant, the breakthrough has distended characteristics; this has the effect of reducing the productivity of pure gases. For Co Formate,[6] for example, intra-crystalline diffusion effects are particularly significant for Xe; this has the effect of reducing the productivity of pure Kr. (Figure S10)

Let us arbitrarily assume that the desired product Kr should have a purity corresponding to 1000 ppm Xe. Corresponding to this purity requirement we can determine the dimensionless breakthrough time, τ_{break}, at which the operation of the fixed bed needs to be stopped and regeneration started to recover pure Xe. From a material balance we can determine the productivity of Kr during the time interval 0 - τ_{break}. The productivities, expressed as mol of pure Kr produced per L of MOF are plotted in Figure S13 as a function of the dimensionless breakthrough time, τ_{break}. The MOF with the highest productivity is Ag@NiMOF-74. The productivity of SBMOF-2 is slightly below that of Co formate.

Notation:

b_A	dual-Langmuir-Freundlich constant for species i at adsorption site A, $Pa^{-\nu i}$
b_B	dual-Langmuir-Freundlich constant for species i at adsorption site B, ${}_{i}Pa^{-\nu i}$
c_i	molar concentration of species i in gas mixture, mol m^{-3}
c_{i0}	molar concentration of species i in gas mixture at inlet to adsorber, mol m^{-3}

Đ_i	Maxwell-Stefan diffusivity, $m^2\ s^{-1}$
L	length of packed bed adsorber, m
n	number of species in the mixture, dimensionless
p_i	partial pressure of species i in mixture, Pa
p_t	total system pressure, Pa
q_i	component molar loading of species i, mol kg^{-1}
r_c	radius of crystallite, m
R	gas constant, 8.314 J $mol^{-1}\ K^{-1}$
t	time, s
T	absolute temperature, K
u	superficial gas velocity in packed bed, m s^{-1}

Greek letters

ε	voidage of packed bed, dimensionless
ρ	framework density, kg m^{-3}
τ	time, dimensionless

Subscripts

i	referring to component *i*
t	referring to total mixture

III. Figures and Tables

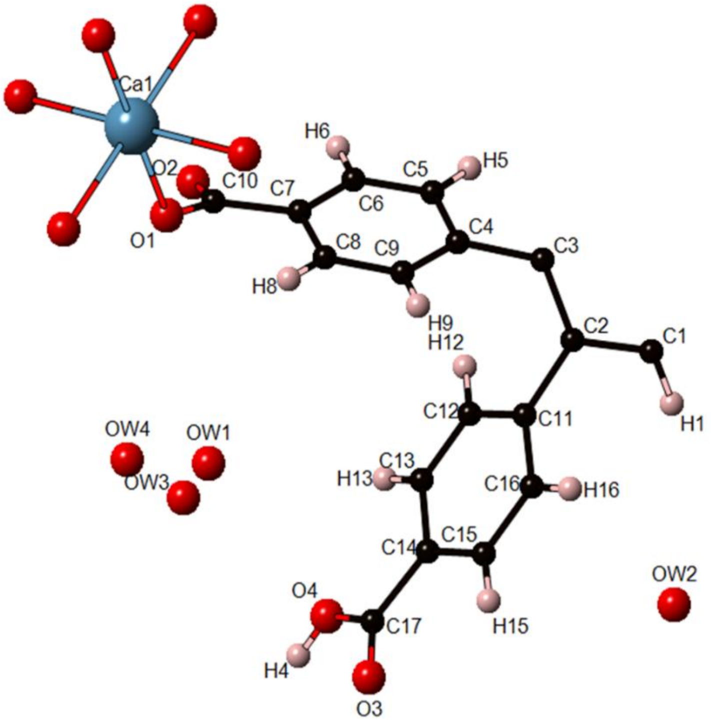

Figure S1. Asymmetric unit of SBMOF-2:H_2O, oxygen atoms coordinating to Ca were duplicated to fill the coordination sphere.

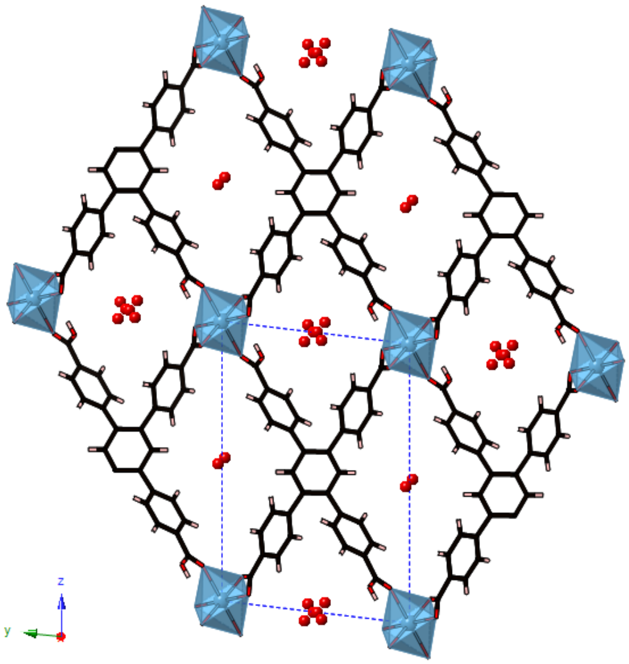

Figure S2. Structure of SBMOF-2:H_2O in [100]. (black sphere/stick represent carbon atoms/carbon bond, red sphere – oxygen, pink – hydrogen and blue – calcium).

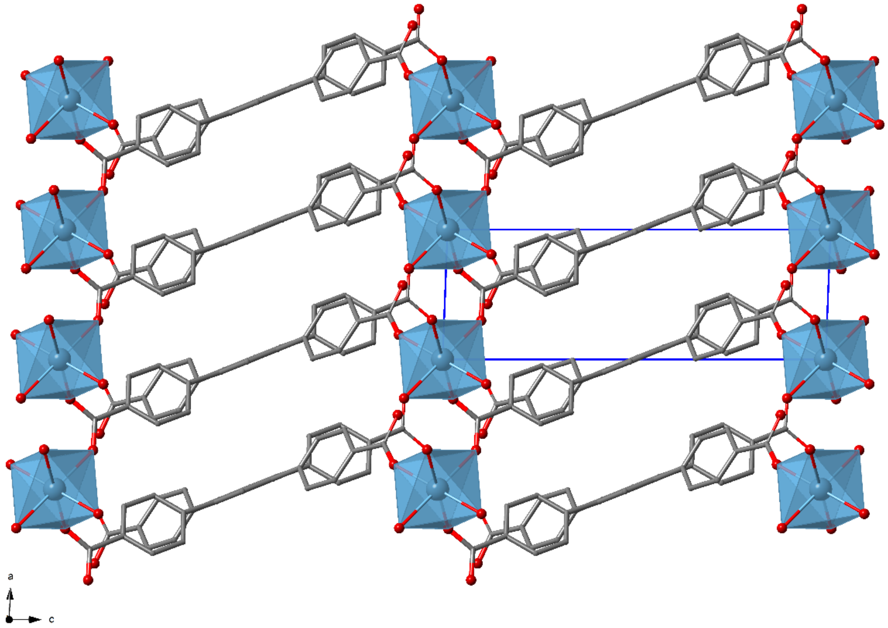

Figure S3. Structure of SBMOF-2:H2O in [010]. (black sphere/stick represent carbon atoms/carbon bond, red sphere – oxygen and blue – calcium. Hydrogen atoms are omitted for clarity)

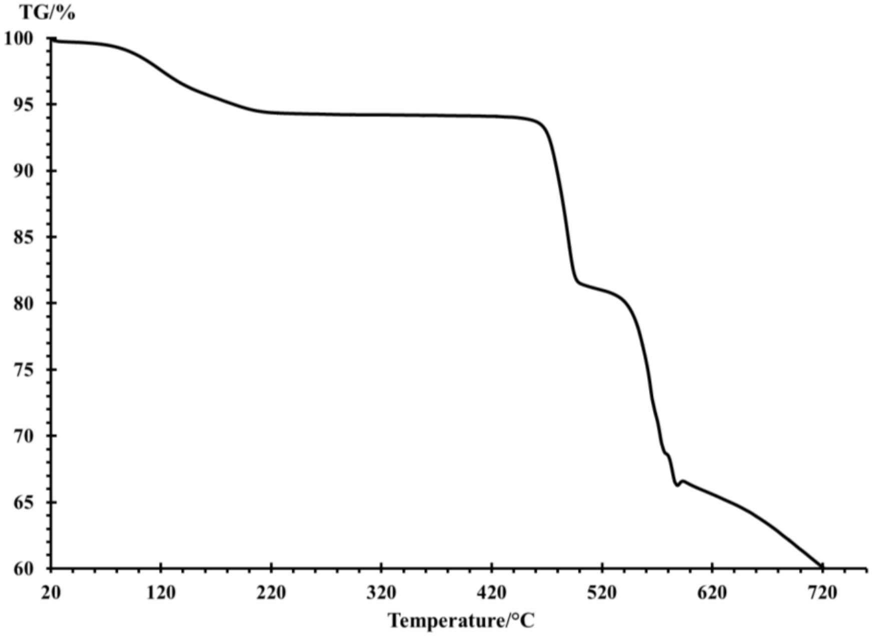

Figure S4. TGA plot of as-synthesized SBMOF-2:H_2O.

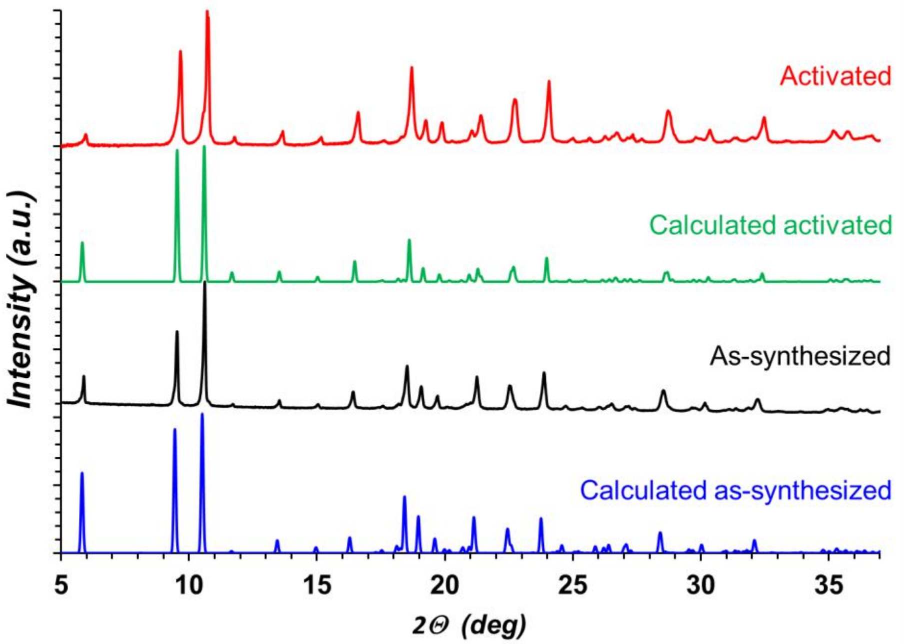

Figure S5. PXRD pattern of experimental and calculated, fresh and activated SBMOF-2.

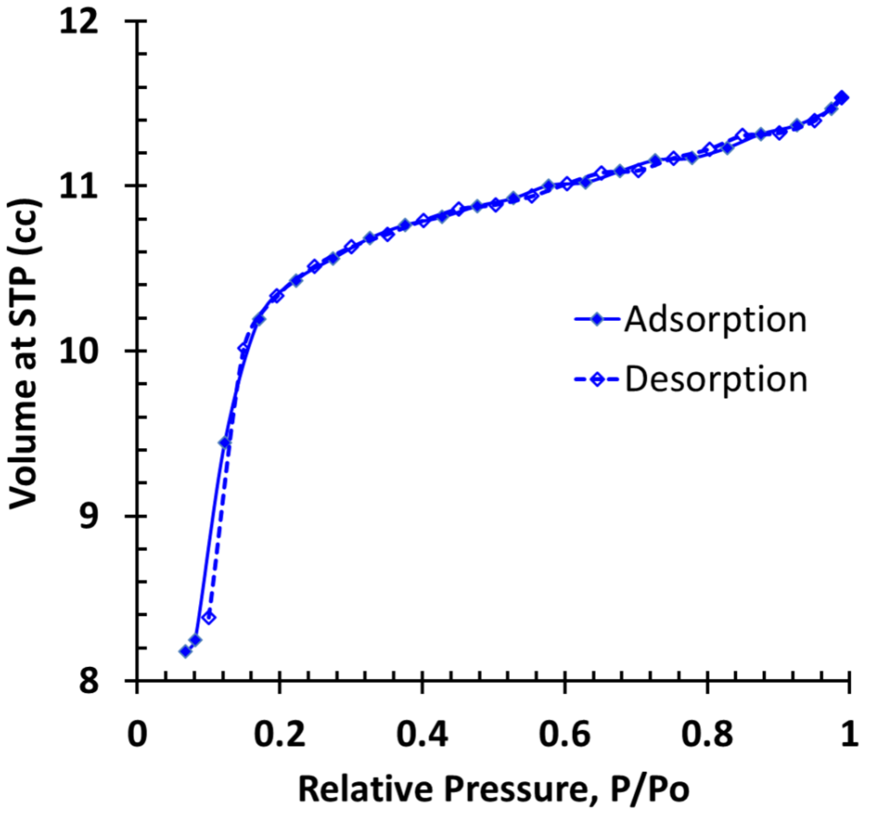

Figure S6. Single component adsorption isotherms (solid symbols) and desorption isotherms (open symbols) of N_2 in SBMOF-2 collected at 77 K.

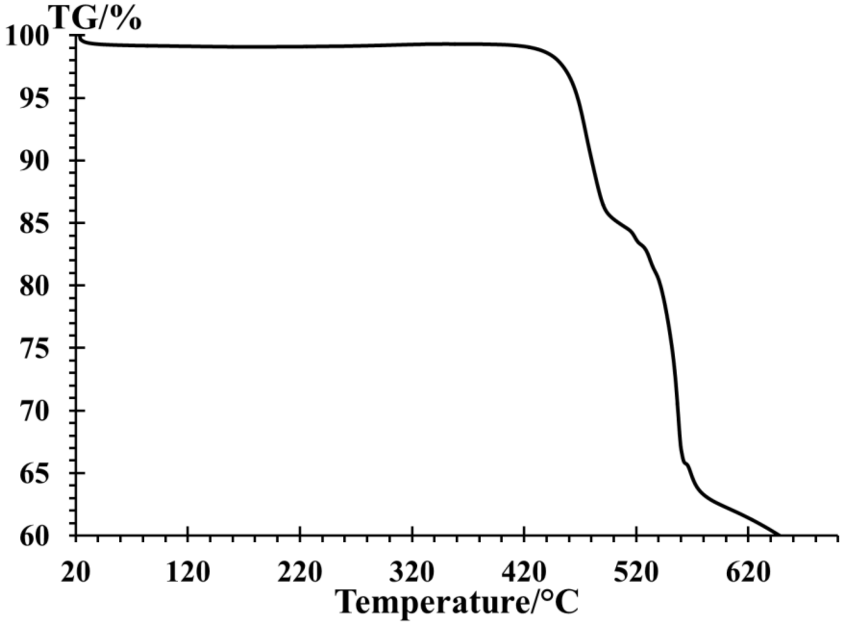

Figure S7. TGA plot of SBMOF-2 after exposing to air for 5 days.

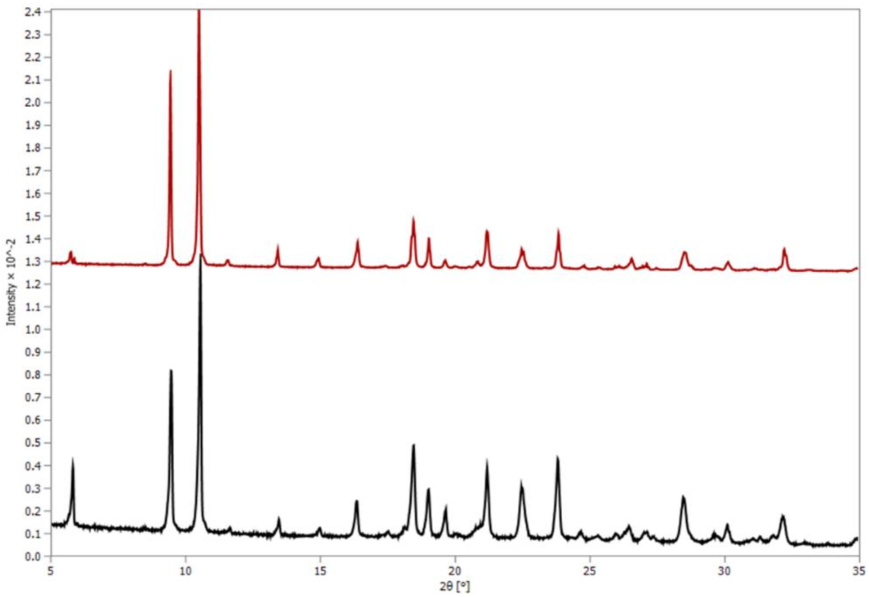

Figure S8. PXRD patterns of SBMOF-2 (black) and SBMOF-2 exposed to 100% humidity conditions for 5 days (red).

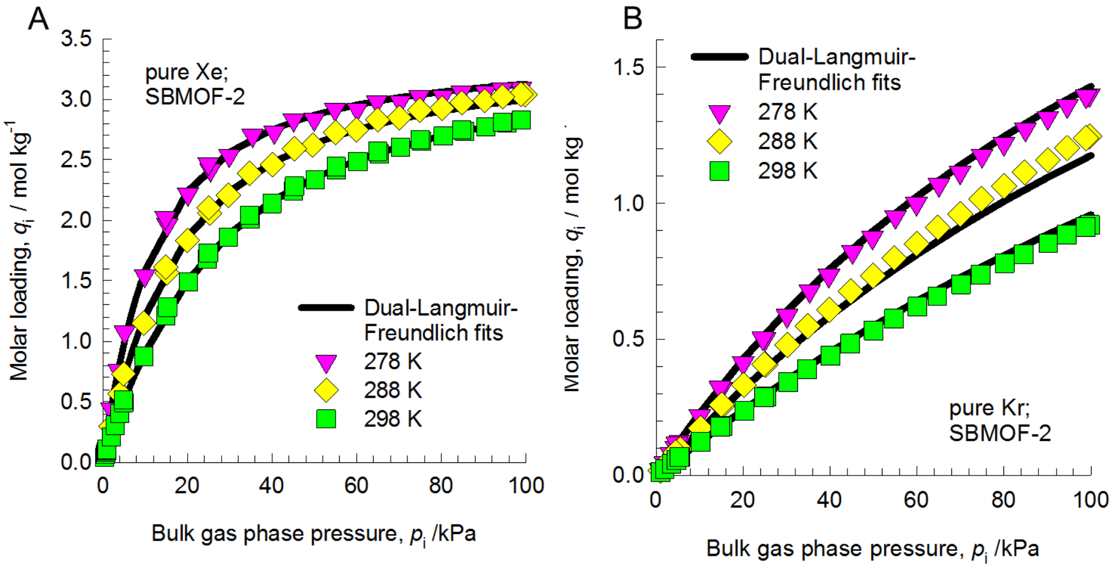

Figure S9. Comparison of the pure component isotherm data for (A) Xe, (B) Kr in SBMOF-2 with the fitted isotherms (shown by continuous solid lines) at 278 K, 288 K, and 298 K. The Langmuir-Freundlich fit parameters are provided in Table S2.

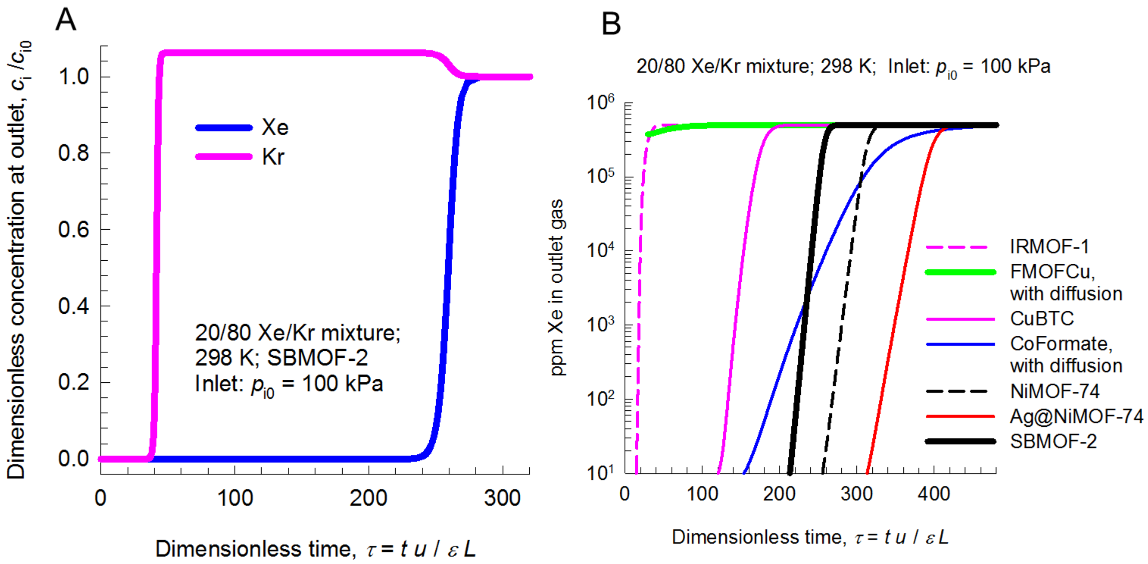

Figure S10. (A) Breakthrough characteristics of 20/80 Xe/Kr mixtures in fixed beds packed with SBMOF-2, operating at 100 kPa at 298 K. For the breakthrough simulations reported here we use the parameter values: L = 0.3 m; voidage of bed, ε = 0.4; interstitial gas velocity, v = 0.1 m/s; superficial gas velocity, u = 0.04 m/s. (B) The ppm Xe in the outlet gas mixture with feed gas of 20/80 Xe/Kr in fixed beds packed with SBMOF-2 and comparison with other compounds.[7]

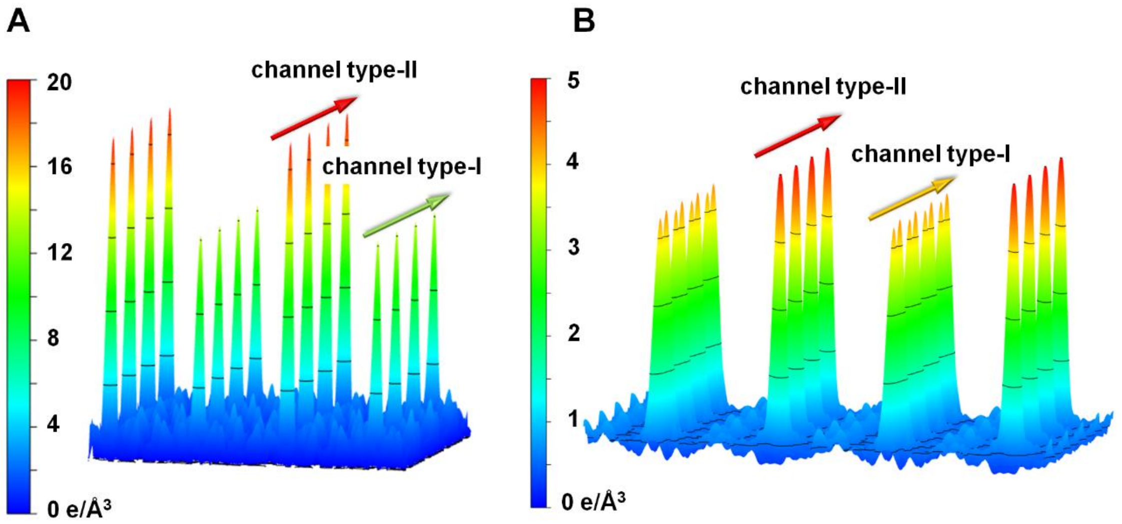

Figure S11. (A) 3D electron-density distribution map derived from single crystal XRD data for SBMOF-2:Xe. Contours are plotted with an interval of 4e/Å^3. (F) 3D electron-density distribution map derived from single crystal XRD data for SBMOF-2:Kr. Contours are plotted with an interval of 1.0 e/Å^3.

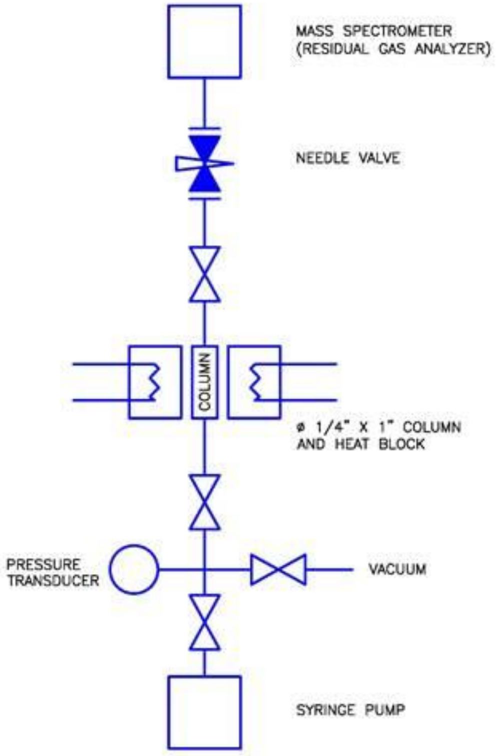

Figure S12. Schematic diagram of breakthrough analysis coupled with residual gas analyzer.

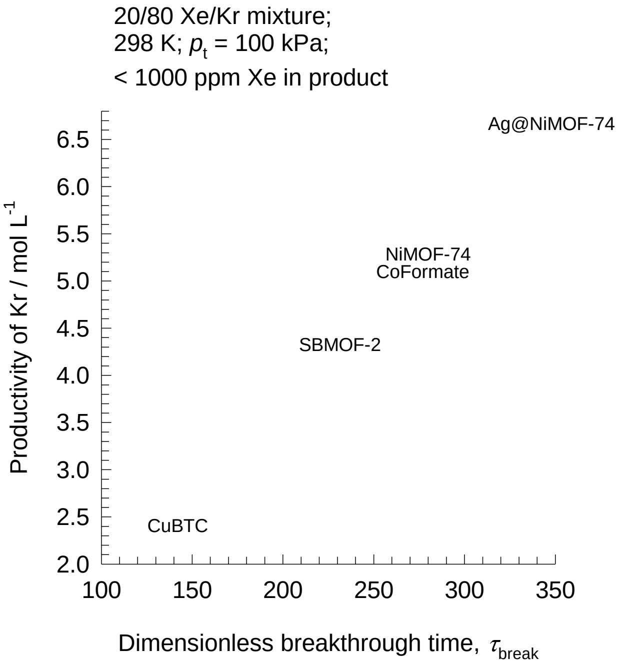

Figure S13. Dependence of the productivity of pure Kr (with < 1000 ppm < Xe), expressed in mol of product per L of MOF, as a function of the dimensionless breakthrough time, τ_{break}.

Table S1 Crystallographic data of as-synthesized, activated, Xe and Kr loaded SBMOF-2

	As-synthesized	Activated	Xe loaded	Kr loaded
Empirical formula	$CaC_{34}H_{20}O_{10.66}$	$CaC_{34}H_{20}O_8$	$CaC_{34}H_{20}O_8 \cdot Xe_{1.45}$	$CaC_{34}H_{20}O_8 \cdot Kr_{0.51}$
T/K	293(2)	100(2)	100(2)	100(2)
λ (Å)	0.71073	0.71073	1.54184	1.54184
a (Å)	5.1594(2)	5.1011(3)	5.1812(3)	5.1161(3)
b (Å)	11.0274(6)	10.8715(9)	10.7420(6)	10.8239(4)
c (Å)	15.2740(8)	15.2363(8)	15.1224(6)	15.2598(4)
α (°)	83.310(4)	83.132(5)	82.466(4)	82.990(2)
β (°)	87.657(4)	85.982(4)	84.928(4)	85.885(3)
γ (°)	83.128(4)	83.032(5)	82.691(5)	83.050(4)
Volume(Å^3)	856.57(7)	831.37(10)	825.41(7)	832.16(6)
Density$_{cacl}$(g/cm^3)	1.239	1.192	1.583	1.277
Mu (mm^{-1})	0.238	0.235	13.489	2.831
Reflections, unique	3502	4125	3377	3525
Reflections, observed[*I>2σ(I)*]	2610	2894	2731	3074
R_{int}	0.0479	0.0815	0.0481	0.0581
Completeness to θ_{max}	0.998	0.999	0.996	0.992
F(000)	329	308	386	326
Goodness of fit	0.895	1.018	1.03	1.067
Data/restraints/parameter	3502/1/216	4125/0/196	3377/0/210	3525/0/210
R_1[*I>2σ(I)*]	0.0440	0.0523	0.0423	0.0483
R_1[all data]	0.0657	0.0854	0.0568	0.0562
wR_2 [all data]	0.1242	0.1358	0.1112	0.1328

Table S2 Dual-Langmuir-Freundlich parameters for adsorption of Xe and Kr in SBMOF-2.

	Site A				Site B			
	$q_{\mathrm{A,sat}}$ mol kg^{-1}	b_{A0} $\mathrm{Pa}^{-\nu_i}$	E_{A} kJ mol^{-1}	ν_{A} dimensionless	$q_{\mathrm{B,sat}}$ mol kg^{-1}	b_{B0} $\mathrm{Pa}^{-\nu_i}$	E_{B} kJ mol^{-1}	ν_{B} dimensionless
Xe	0.23	2.54×10^{-9}	29.3	0.95	3.13	1.12×10^{-11}	32.2	1.2
Kr	1.73	5.52×10^{-11}	20.3	1.2	1.81	4.66×10^{-10}	23.4	1

IV. References

(1) Sheldrick, G. M. *Acta Crystallogr. A* **1990**, 46, 467.
(2) Sheldrick, G. M. *SHELXL-97* (University of Göttingen, **1997**).
(3) Myers, A. L.; Prausnitz, J. M. *A.I.Ch.E.J*. **1965**, 11, 121.
(4) Krishna, R.; Long, J. R. *J. Phys. Chem. C* **2011**, 115, 12941.
(5) Krishna, R. *Micropor Mesopor Mat* **2014**, 185, 30.
(6) Wang, H.; Yao, K.; Zhang, Z.; Jagiello, J.; Gong, Q.; Han, Y.; Li, J. *Chem. Sci.* 2**014**,5, 620
(7) Banerjee, D.; Cairns, A. J.; Liu, J.; Motkuri, R. K.; Nune, S. K.; Fer-nandez, C. A.; Krishna, R.; Strachan, D. M.; Thallapally, P. K. *Acc. Chem. Res*. **2015**, 48(2), 211.